Materials Advances

ROYAL SOCIETY OF CHEMISTRY

PAPER

View Article Online
View Journal | View Issue

Open Access Article. Published on 07 August 2025. Downloaded on 1/7/2026 11:10:38 PM.
This article is licensed under a Creative Commons Attribution-NonCommercial 3.0 Unported Licence.

Check for updates

Cite this: *Mater. Adv.*, 2025, **6**, 6345

Lithium recovery using a spinel-type hydrogen manganese oxide (HMO)–SBA-15 nanocomposite†

Keivan Sohrabpour,* Antonio Grisolia, Francesco Chidichimo, Pietro Argurio, Efrem Curcio, Salvatore Straface‡ and Luigi Pasqua‡

Received 9th May 2025,
Accepted 22nd July 2025

DOI: 10.1039/d5ma00467e

rsc.li/materials-advances

In today's economy, lithium is a crucial material, especially for electric vehicles (EVs) and renewable energy storage systems, which highlights the need for a more efficient and sustainable extraction method. There are well-established traditional methods such as brine evaporation and mineral processing, but they are time consuming, resource-intensive, and environmentally damaging. To address these issues, numerous methods have been proposed, and adsorption has emerged as a promising alternative. In this study, we report the development of a novel nanocomposite material (HMO-SBA15) synthesized *via* a straightforward and scalable route, starting from Santa Barbara amorphous (SBA) mesoporous silica and hydrogen manganese oxide (HMO), for the selective capture of lithium. HMO–SBA15 was synthesized by incorporating $Li_4Mn_5O_{12}$ into $SBA15_{calc}$, followed by H^+ exchange to form a lithium ion-sieve (LIS) to capture lithium from an aqueous solution. The material was characterized by SEM, TEM, nitrogen adsorption–desorption analysis, FTIR, XRD, and TGA. Adsorption was evaluated under different conditions, namely pH, initial lithium concentrations, and contact time. The maximum adsorption capacity of 14.2 mg g^{-1} was achieved after 6 hours at pH $\sim$ 7 and C_0 = 350 mg L^{-1}. Through kinetic and isotherm studies it was shown that the adsorption process followed a pseudo-second-order model, and the Langmuir isotherm best described the adsorption behavior, indicating monolayer adsorption. We demonstrated that the HMO–SBA15 composite has the potential to recover lithium from an aqueous solution and, with high surface area, structural stability, and operating at near-neutral pH, may be a sustainable and environmentally friendly alternative to traditional lithium extraction materials.

1. Introduction

Lithium's unique properties make it essential for advanced technologies, especially in renewable energy and electric mobility. The global demand has surged over the past few decades, driven by electric vehicles, portable electronics, and energy storage systems. This highlights the need for efficient, sustainable lithium extraction methods to meet future requirements.[1,2]

The global push towards decarbonization and sustainable energy solutions has highlighted lithium as a cornerstone element.[3] Lithium-ion batteries power devices like smartphones, laptops, EVs, and large-scale energy storage devices. They are vital for renewable energy, efficiently storing solar and wind power to balance supply and ensure stable output.[4] This ability to store and deliver energy on demand makes lithium essential in mitigating the intermittent nature of renewable energy sources. Beyond energy storage, lithium also finds applications in the pharmaceutical industry, where it is used in the treatment of bipolar disorder,[5–7] and in the manufacture of high-performance alloys and ceramics.[8,9]

Traditional methods of lithium extraction include brine evaporation and mineral processing. Brine evaporation involves pumping lithium-rich brine from underground reservoirs into large evaporation ponds. Over a period of 12 to 18 months, solar energy is used to evaporate the water, concentrating the lithium. This method is predominantly used in regions like the Atacama Desert in Chile and the Salar de Uyuni in Bolivia, where climatic conditions favor rapid evaporation. However, this method has several drawbacks, including high water consumption, long processing times, and significant environmental impact due to the large land areas required for evaporation ponds.[10,11] Mineral processing, on the other hand, involves extracting lithium from hard rock minerals such as spodumene. This method is energy-intensive, requiring extensive crushing, grinding, and high-temperature roasting to convert spodumene into a form that can be processed. While this method can produce high-purity lithium, it is costly and has a significant carbon footprint.[10,12,13]

Department of Environmental Engineering, DIAm, University of Calabria, Via Pietro Bucci CUBO 44/A, 87036 Rende, CS, Italy. E-mail: Keivan.sohrabpour@unical.it

† Electronic supplementary information (ESI) available. See DOI: https://doi.org/10.1039/d5ma00467e

‡ These authors share the last authorship.

© 2025 The Author(s). Published by the Royal Society of Chemistry

Open Access Article. Published on 07 August 2025. Downloaded on 1/7/2026 11:10:38 PM. This article is licensed under a Creative Commons Attribution-NonCommercial 3.0 Unported Licence.

Given the limitations of these traditional methods, there is growing interest in developing more efficient and sustainable extraction techniques. There are several methods tested for lithium recovery, such as solvent extraction,[14] sorption and ion-exchange methods,[15] zeolites,[16] and membrane-based processes.[17] Membrane techniques, such as nanofiltration (NF), electrodialysis (ED), and forward osmosis (FO), have shown potential for lithium extraction from high magnesium–lithium ratio (MLR) brines, offering selective ion separation based on size and charge. However, large-scale production and maintaining selectivity pose challenges, and the high costs associated with membrane performance limit their practicality.[17,18] Among these, adsorption methods have emerged as a promising alternative. Adsorption techniques offer several advantages over traditional lithium extraction methods. One of the primary benefits is higher selectivity for lithium ions. Adsorbent materials, such as lithium ion sieves, are designed to preferentially capture lithium ions from a mixture of different cations.[19] Adsorption methods also have lower energy consumption compared to traditional techniques. They can operate at ambient temperatures and pressures, significantly reducing the energy requirements and associated costs.[20–23] This makes adsorption a more environmentally friendly option, aligning with global sustainability goals by minimizing carbon emissions and reducing the environmental footprint of lithium extraction.

Santa Barbara amorphous (SBA) materials, like SBA-15, feature a highly ordered mesoporous structure, large diameter pores, and high surface areas, ideal for ion exchange and lithium adsorption from different sources.[24] These properties boost efficiency, making SBA-15 key for ion sieve development. HMO's layered structure and high ion-exchange capacity, combined with SBA-15, allow selective lithium trapping, enhancing the composite's performance.[25–28]

The combination of SBA-15's mesoporosity and HMO's ion selectivity creates a synergistic effect, boosting lithium adsorption. While HMO captures lithium *via* electrostatic interactions, its low surface area limits capacity. Mounting HMO on SBA-15 enhances adsorption capacity, selectivity, and kinetics through SBA-15's high surface area. This hybrid improves isotherm fitting, stability, and reusability, making it ideal for lithium capture and recovery.

The objective of this research is to develop a composite material that combines the advantageous features of both SBA-15 and HMO, aiming to create an efficient ionic sieve for lithium ion capture. By embedding HMO within the SBA-15 framework, we aim to leverage the structural integrity and mesoporosity of SBA-15.[29] The composite synthesizing process involves incorporating the spinel-type crystal structures of $LiCl_2$ and MnO_2 into SBA-15, followed by calcination and H^+ exchange, which promotes the formation of an effective adsorbent for lithium ions. Furthermore, this study describes the lithium capture ability of the developed HMO–SBA-15 composite under varying pH conditions and at initial concentrations of Li^+. We assess key parameters such as isotherms and kinetic models to provide a comprehensive understanding of the capture mechanism and its efficiency. By defining these objectives and rationale in detail, this work combines materials science with environmental engineering, to develop an efficient nanocomposite-based lithium recoverability method. This work provides both fundamental contributions and significant potential for achieving resource sustainability and circular economy goals.

2. Materials and methods

2.1. Materials and reactants

LiCl (lithium chloride, anhydrous, free-flowing, Redi-DriTM, ReagentPlus® = 99.0% (AT), Mfr. No. 793620-1KG), tetraethylorthosilicate (TEOS), HCl (37%), Pluronic P-123, manganese chloride tetrahydrate ($MnCl_2{\cdot}4H_2O$), and ethanol were purchased from Sigma Aldrich and deionized water (5.5 μS m^{-1}) produced by PURELAB (Elga LabWater, UK) was used throughout the adsorption experiments. All other chemicals and reagents were used without further purification.

2.2. Nanocomposite

2.2.1 Synthesis of HMO-loaded mesoporous SBA15 (HMO–SBA15). The preparation of pure silica SBA15 samples and HMO–SBA15 followed the method from ref. 30 and 31 respectively. First, 4 g of Pluronic P-123 was dissolved in 120 g of ultrapure water and 24 g of HCl (37%) until completely dissolved. Next, 8.5 g of TEOS was added dropwise, and the mixture was stirred at 300 rpm and 313 K for 24 hours before aging at 353 K for 2 days. The sample was filtered under vacuum, washed with 50 mL of ethanol three times and dried at 363 K overnight. The resulting $SBA15_{AS}$ underwent calcination by heating 8 g of it in a muffle furnace from 30 °C to 550 °C at 100 °C h^{-1} and held at 550 °C for 3 hours to yield $SBA15_{calc}$. Five grams of $SBA15_{calc}$ were mixed with 100 mL of a 1 : 1 Li/Mn ethanol solution, retaining a Li : Mn : Si mole ratio of 1 : 1 : 10, and heated at 60 °C for 30 hours. The mixture was then filtered and dried at 80 °C overnight, followed by calcination at 500 °C for 8 hours to obtain the LMO–SBA15 sample. Finally, LMO–SBA15 was dissolved in 100 mL of 0.3 M HCl for 24 hours, acidifying and allowing the substitution of lithium ions in the crystal cage with protons, filtered, and dried at 80 °C overnight to obtain HMO–SBA15.

2.2.2 Characterization methods. Thermogravimetric analysis (TGA) was carried out using a Netzsch STA 449 system, covering a temperature range from 293.15 K to 1123.15 K, with a heating rate of 1 K per minute under an air atmosphere at a flow rate of 10 mL min^{-1}. Scanning electron microscopy (SEM) images were acquired using an ultra high-resolution SEM (UHR-SEM) – ZEISS CrossBeam 350 at various magnifications. Transmission electron microscopy (TEM) images were obtained with a Jeol 1400 Plus electron microscope, operating at an acceleration voltage of 80 kV. Fourier transform infrared (FT-IR) spectroscopy was carried out using an FT/IR-4600 spectrometer (Jasco, Germany). The specific surface area and average pore size of all samples were determined using the Brunauer–Emmett–Teller (BET) method, based on nitrogen adsorption measurements with a Micromeritics Tristar II Plus system. Prior to analysis, samples were degassed at 120 °C for

 © 2025 The Author(s). Published by the Royal Society of Chemistry

Open Access Article. Published on 07 August 2025. Downloaded on 1/7/2026 11:10:38 PM.
This article is licensed under a Creative Commons Attribution-NonCommercial 3.0 Unported Licence.

150 minutes using a Micromeritics FlowPrep 060 degassing system. X-ray diffraction (XRD) measurements were performed using a Rigaku MiniFlex diffractometer. Scans were conducted over two ranges: $0.3 < 2\theta < 10^\circ$ and $10 < 2\theta < 90^\circ$, at a scan rate of 0.005° per second.

2.3 Batch adsorption of lithium

A lithium stock solution of 1000 ppm was prepared by adding 6.1208 g of LiCl to a 1 L volumetric flask. To achieve varying concentrations, the requisite volume of this solution was diluted with ultrapure water. The adsorptive batch studies were performed at room temperature (293 ± 1 K) in 20 mL glass bottles. The parameters investigated for the adsorption tests included pH, contact time, and initial lithium concentration. To determine the optimum pH, various vials containing a fixed solution and adsorbent at different pH levels were stirred (MediLab Tech Magnetic Stirrer, DLAB MS-H380-Pro-China) for 24 hours (pH adjustments within the adsorption system were achieved by the addition of either 0.1 M NaOH (VWR Chemicals) or 0.1 M HCl (Carlo Erba Reagents) to attain the desired values). The samples were then filtered through a 0.22 μm syringe filter (VWR International), and atomic absorption (Analytik Jena, contrAA 700, Germany) was used to measure the remaining lithium concentration. The pH with the highest adsorption capacity was selected for subsequent experiments. For contact time and initial lithium concentration effects, a known amount of adsorbent was added to each bottle containing 20 mL of Li^+ at the desired concentration. The capped bottles were stirred for specific durations at 350 rpm and filtered afterward, and the remaining lithium was quantified using atomic absorption. Additionally, for the investigation of adsorption kinetics and isotherms, equilibrium adsorption data from contact time and initial lithium concentration were utilized. The percentage of lithium removal was calculated following the method described by Anantha *et al.*[32] according to eqn (1):

$$\text{Removal}\ (\%) = \left[\frac{C_0 - C_e}{C_0}\right] \times 100 \tag{1}$$

where C_0 and C_e are the initial and equilibrium lithium concentrations (mg L^{-1}), respectively. The amount of lithium ions adsorbed at equilibrium by the mass of adsorbent was calculated using the following equation (eqn (2)):[33]

$$Q_e = (C_0 - C_e) \times \frac{V}{W} \tag{2}$$

where Q_e is the equilibrium adsorption capacity (mg g^{-1}), V is the volume of the solution (L) and W is the adsorbent mass (g). The distribution coefficient (K_d) and the separation factor (α_M^{Li}) are adopted to evaluate the selectivity of our nanomaterial toward Li^+ in comparison to other cations and are calculated using the following equations:[34]

$$\begin{aligned} K_d &= (C_0 - C_e) \times \frac{V}{C_e W} \\ \alpha_M^{Li} &= \frac{K_{Li}}{K_d} \quad M = (\text{Li, Na, K, Ca, Mg}) \end{aligned} \tag{3}$$

To investigate these parameters, we used a semi-real brine composition to get a rather realistic view of the performance of our material. The composition of brine was according to ATACAMA brine composition in ref. 35, in a 20 mL glass vial for 6 h at neutral pH. The composition is indicated in Table S1 in the ESI.†

2.4 Adsorption isotherms

In this work, two isotherm models, Langmuir and Freundlich, were employed to identify the optimal model for characterizing the adsorption process, based on insights from previous studies.[36–38] The Freundlich isotherm is as follows:

$$Q_e = K_f C_e^{\frac{1}{n}} \tag{4}$$

where K_f is the Freundlich constant ($L^{1/n}\ g^{-1}\ mg^{-(1/n-1)}$) and $\frac{1}{n}$ is the adsorption intensity. The second isotherm law analyzed in this work is the Langmuir isotherm. It is represented by eqn (5):

$$Q_e = \frac{Q_{max} K_L C_e}{1 + K_L C_e} \tag{5}$$

where Q_{max} is the theoretical maximum adsorption capacity of HMO–SBA15 (mg g^{-1}) and K_L is the Langmuir constant (L mg^{-1}).

2.5 Adsorption kinetics

Adsorption kinetics is calculated using pseudo-first order and pseudo-second order kinetics models.[39,40] The pseudo-first order kinetics assumes that the rate of change of the adsorption capacity is proportional to the concentration of available active sites per unit mass of the adsorbent material:[41]

$$\frac{dQ_t}{dt} = k_1(Q_e - Q_t) \tag{6}$$

where Q_t represents the adsorption capacity (mg g^{-1}) at time t while K_1 (min^{-1}) is the pseudo-first order constant. In addition, the pseudo-second order rate equation[42] can be written as:

$$\frac{dQ_t}{dt} = k_2(Q_e - Q_t)^2 \tag{7}$$

where k_2 is the pseudo-second order rate constant (g mg^{-1} min^{-1}). The most suitable isotherm and kinetic laws will be determined by means of the least square error (LSE) method.

2.5.1 Reversible kinetics for the evaluation of desorption processes. A mathematical model describing reversible second order adsorption kinetics[43] has been adopted in this study, in order to analyze batch experiments and investigate the adsorption–desorption processes of water dissolved lithium onto the reactive porous material. The implemented model features the progressive reduction of the recovery capacity of the material due to the gradual exhaustion of the active sites available for solute retention.

The second order reversible model describing the time variation of the solute concentration during a batch test is given by the following equation:

$$C(t) = \frac{S_2 - S_1 e^{[\Delta - K_1 t(S_2 - S_1)]}}{1 - e^{[\Delta - K_1 t(S_2 - S_1)]}} \tag{8}$$

Open Access Article. Published on 07 August 2025. Downloaded on 1/7/2026 11:10:38 PM.
This article is licensed under a Creative Commons Attribution-NonCommercial 3.0 Unported Licence.

where:

$$\Delta = -\ln\frac{(S_1 - C_0)}{(S_2 - C_0)}$$

$$\begin{cases} S_1 = \dfrac{-\beta + \sqrt{\beta^2 - 4\gamma}}{2} \\ S_2 = \dfrac{-\beta - \sqrt{\beta^2 - 4\gamma}}{2} \end{cases}$$

$$\begin{cases} \beta = C_0 - aF_0 - \dfrac{K_2}{K_1} \\ \gamma = -\dfrac{K_2}{K_1}C_0 \end{cases}$$

and C_0 (mg L^{-1}) is the batch initial concentration. It can be used to estimate the adsorption/desorption kinetic constants of the reactive material K_1 (L mg^{-1} min^{-1}) and K_2 (min^{-1}) and the initial concentration F_0 (mg g^{-1}) of active sites (the maximum absorbable amount of pollutant per unit of adsorbent mass or maximum adsorption capacity), by fitting the experimental data. The conversion factor a (g L^{-1}) is the ratio of the mass of the porous adsorbent material to the solution volume used for the batch preparation.

3. Results and discussion

3.1 Development strategy of the nanocomposite HMO–SBA-15

The LMO–SBA15 sample has been obtained by adding lithium ($LiCl{\cdot}H_2O$) and manganese ($MnCl_2{\cdot}4H_2O$) salts to silica nanoparticle dispersion to induce the formation of the spinel-type crystal structure $LiMn_2O_4$. Successively, the Li^+ ions are replaced with H^+ ions.[44] Spinel-type crystal structures represent a significant class of crystalline materials commonly found in both natural minerals and synthetic compounds. They present a cubic crystal system, with a characteristic unit cell arranged in a dense, compact configuration,[45] and are known for their high stability, attributed to their symmetrical and compact arrangement. This stability, along with other unique properties, makes spinel-type materials valuable in various applications, including catalysis and lithium adsorption.[46–48] The nanomaterial SBA15 serves as a stable, chemical and thermally resistant support, enabling the formation of spinel-type structures on its surface. These spinel structures are the active agents responsible for lithium adsorption. When the nanomaterial is subsequently used for Li adsorption, the reverse ion-exchange reaction takes place, reintegrating the Li^+ ions back into the crystal structure. This process also allows for the recycling of adsorbent nanomaterials. This system, developed using SBA15 as a support, introduces aspects that differentiate it from previously described approaches. The highly ordered, uniform pore structure of SBA15 enables precise control over porosity and pore size, which could enhance lithium-ion diffusion and retention efficiency. Moreover, its linear structure contributes to an extensive surface area, which may enhance adsorption efficiency. SBA15 also demonstrates notable chemical resilience in challenging environments, such as acidic or basic conditions. Additionally, the synthesis process for SBA15 tends to be straightforward and scalable, potentially offering a more cost-effective pathway for applications on a larger scale. Importantly, the material synthesized using SBA15 is environmentally friendly because the synthesis process avoids the use of dangerous reactants or harsh conditions. Furthermore, the template used in its production could potentially be extracted and recycled. This contributes to an economically sustainable approach, as the synthesis is not only simple and cost-effective but also enables the recycling of the material. Finally, the process is highly scalable, as the same synthesis protocol can be used to obtain larger quantities of nanomaterials, which reinforces its potential for broader industrial applications. In Scheme 1 the development process of the material HMO–SBA15 is reported.

3.2 $SBA15_{AS}$ and $SBA15_{calc}$ characterization

Both the as-synthesized and calcined SBA15 samples (Fig. 1a and b) exhibit a well-defined arrangement of longitudinal porous structures. The channels within these structures appear as parallel stripes, a hallmark of this family of silica nanomaterials.[50] The pores are likely cylindrical in shape and are organized in a 2-D hexagonal pattern.[51] The morphology observed in the synthesized SBA15 can likely be attributed to the specific synthesis parameters employed, consistent with findings reported in previous studies.[52,53]

3.2.1 TG-DSC and the XRD graph. The $SBA15_{calc}$ sample (Fig. S1, ESI†) exhibits two prominent peaks at approximately 0.62 and 0.88 degrees 2-theta, corresponding to the (100) and (110) planes, respectively. This indicates a hexagonal symmetry with the *P6mm* space group, a characteristic observed exclusively in the thermally treated sample.[54,55] In contrast, because of the presence of the surfactant, the AS sample (Fig. S1, ESI†) shows only a single peak (100). Fig. S2 (ESI†) shows the thermogravimetric analysis (TGA) of the nanomaterials at a heating rate of 1 K min^{-1}. The $SBA15_{AS}$ samples (Fig. S2a, ESI†) exhibit a 35% mass loss from 25 to 950 °C, mainly due to organic template decomposition. The differential scanning calorimetry (DSC) graph for $SBA15_{AS}$ indicates an exothermic peak around 150 °C (Fig. S2a, ESI†), which corresponds to surfactant removal. The organic/SiO_2 mass ratio is 30.34%. In the calcined samples (Fig. S2b, ESI†), mass loss drops to about 2.13% from 100 to 948 °C, attributed to the condensation of surface hydroxyl groups.

3.3 LMO and HMO–SBA15 characterization

Spinels, a class of crystalline materials with a general formula AB_2O_4, where A and B represent different metal cations and O represents oxygen, crystallize in a cubic structure, with a closely packed oxygen framework and cations occupying specific interstitial sites. A highly stable and symmetrical arrangement is created with A cations typically occupying tetrahedral sites, while B cations residing in octahedral sites. This unique structure is responsible for the spinels' remarkable stability, making them attractive for various applications in catalysis, magnetic materials, and energy storage systems.[45,56] In the context of lithium adsorption, spinel-type structures, such as lithium manganese oxide ($LiMn_2O_4$), are particularly important due to their ion-exchange capabilities[57] that allow lithium ions

 © 2025 The Author(s). Published by the Royal Society of Chemistry

Open Access Article. Published on 07 August 2025. Downloaded on 1/7/2026 11:10:38 PM.
This article is licensed under a Creative Commons Attribution-NonCommercial 3.0 Unported Licence.

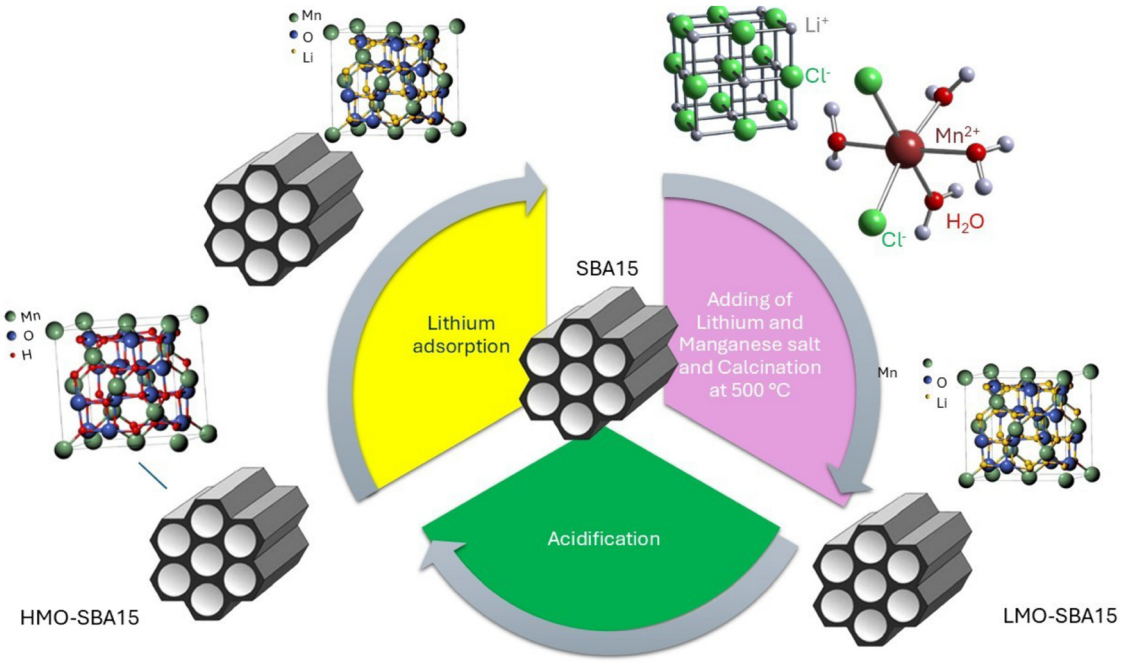

Scheme 1 Schematic representation of the development process of HMO–SBA. (1) Addition of lithium ($LiCl{\cdot}H_2O$) and manganese ($MnCl_2{\cdot}4H_2O$) salts to calcined mesoporous silica nanoparticles ($SBA15_{calc}$).[49] (2) High-temperature calcination to form silica nanoparticles functionalized with spinel crystalline structures, with lithium in tetrahedral and manganese in octahedral coordination respectively. (3) Acidification to facilitate ion exchange between H^+ and Li^+, activating the surface for lithium adsorption. (4) Lithium adsorption through further ion exchange between H^+ and Li^+, resulting in lithium capture on the nanoparticle surface.

to be reversibly intercalated into and extracted from the spinel lattice without significantly disrupting the crystal structure.[31,44] This makes spinels highly effective as ion-sieves for lithium recovery. Selective capture of lithium ions from aqueous solutions occurs by exchanging lithium ions with hydrogen ions in the spinel framework. Moreover, the high surface area and porosity of mesoporous supports, like SBA15, enhance the accessibility of lithium ions to the active spinel sites, further improving the efficiency of adsorption. In this study, the spinel formation on the SBA15 surface enabled the selective and efficient adsorption of lithium ions. We conducted a thorough characterization to examine the structural integration of lithium manganese oxide (LMO) and, after acidification, HMO into the SBA15 framework.

3.3.1 SEM-EDX and TEM analyses. Fig. 2 presents the SEM (Fig. 2a) and TEM (Fig. 2b and c) images of the LMO–SBA15 sample along with EDX analysis, indicating that post-synthesis grafting does not alter the nanomaterial's morphology, which tends to aggregate. EDX (Fig. S3, ESI†) confirms Mn's presence, while lithium remains undetected due to the method's limitations. The nanoparticle in Fig. 2c exhibits dense areas, suggesting an intact crystalline structure with clear lattice fringes, indicative of a well-ordered phase, as shown by atomic adsorption analysis. Fig. 2c displays the HMO sample post-acid treatment, reflecting reduced density in some regions due to lithium-ion extraction.

3.3.2 XRD and atomic adsorption. Fig. S4 (ESI†) shows the XRD plot of the LMO–SBA15 sample at high and low angles. It shows that all diffraction peaks observed can be attributed to the spinel phase of the $LiMn_2O_4$ compound, as confirmed by

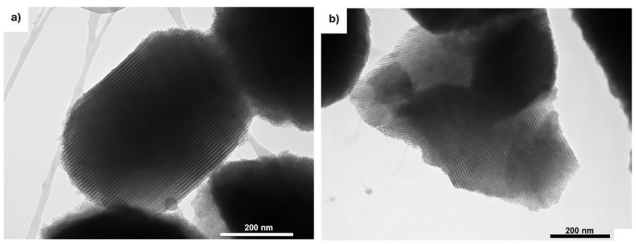

Fig. 1 TEM images of (a) $SBA15_{As}$ and (b) $SBA15_{calc}$.

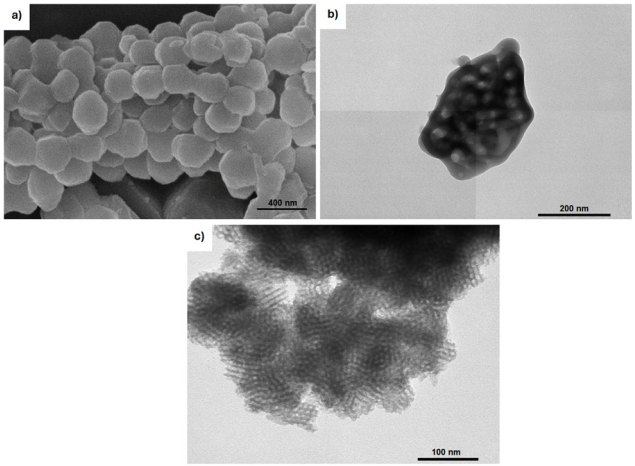

Fig. 2 (a) SEM image of LMO–SBA15, mag 50k×, size bar 400 nm and TEM images of (b) LMO–SBA15, bar length 200 nm and (c) HMO–SBA15, bar length 100 nm.

Open Access Article. Published on 07 August 2025. Downloaded on 1/7/2026 11:10:38 PM.
This article is licensed under a Creative Commons Attribution-NonCommercial 3.0 Unported Licence.

comparison with the standard JCPDS card no. 35-0782.[31,58] The broad peak around 23 2-theta degrees is attributable to the amorphous part of the silica nanoparticle. The LMO spinel-type is successfully loaded on the $SBA15_{calc}$ sample. The atomic adsorption analysis conducted on LMO–SBA15 confirms that the atomic ratio of Li : Mn is nearly 1 : 2. The spinel crystals present a quasi-stoichiometric ratio of $LiMn_2O_4$ as confirmed by the XRD graph. Even after acidification, the XRD pattern of the HMO material shown in Fig. S5 (ESI†) reveals characteristic peaks at approximately 18, 44, and 55 degrees 2θ, although the signal-to-noise ratio remains high.

3.4 N_2 adsorption porosimetry

Fig. 3 shows the nitrogen adsorption–desorption isotherms of the samples $SBA15_{calc}$, HMO–SBA15 and LMO–SBA15 that can be classified according to the IUPAC as type IV not-reversible ones. This is a hallmark of mesoporous materials with a well-organized 3D pore network, such as SBA15.[59]

The porous structure of LMO–SBA15 and HMO–SBA remains unchanged by spinel formation or acidification. LMO–SBA15 shows a smaller average pore size than $SBA15_{calc}$ (Table 1 and Fig. S6a–c, ESI†). A slope drop in the higher-pressure region of LMO–SBA15 and HMO–SBA15 suggests partial pore blockage by spinel crystals, widening the mesopore size distribution and reducing nitrogen adsorption (Fig. S6, ESI†). In HMO–SBA15, acid treatment likely removes loosely bound crystals, increasing surface area. Starting from porosimetric and thermogravimetric considerations, and taking into account that the specific surface area of LMO spinels is on average around 10 $m^2\ g^{-1}$, as reported in ref. 60 and in ref. 61, an SBA/LMO ratio of approximately 70 : 30 was calculated. BET surface area, pore volume, and width are shown in Table 1.

3.5 FTIR

Fig. 4 displays the FTIR spectra of $SBA15_{AS}$, $SBA15_{calc}$, and HMO–SBA15, highlighting SiO_2 vibrational modes. The band at 1111 cm^{-1} relates to asymmetric Si–O–Si stretching, while the band at 819 cm^{-1} indicates symmetric stretching. Si–OH bonds produce a peak at 949 cm^{-1}, and water adsorption is shown by 1636 cm^{-1} (bending) and a broad band around 3300 cm^{-1} (stretching). In $SBA15_{AS}$, the peak at 1353 cm^{-1} is from methyl group bending; 1455 cm^{-1} and 1719 cm^{-1} are assigned to bending and scissoring of methyl and methylene groups, respectively. The 2922 cm^{-1} peak in SBA15AS vanishes in $SBA15_{calc}$. The FT-IR spectra of HMO and LMO overlap with SBA_{calc}, with the LMO spectrum omitted for clarity. The intense Si–O–Si bands may mask the weaker Si–O–Mn band due to similar regions and higher intensity. Incorporating manganese oxide into the SBA15 framework maintains its porous structure, essential for efficient ion exchange. Nitrogen adsorption–desorption analysis indicates that while spinel formation reduces pore size and volume, overall porosity remains adequate for lithium adsorption.[62–65]

Table 1 N_2 adsorption data

Samples	BET surface area ($m^2\ g^{-1}$)	Pore volume ($cm^3\ g^{-1}$) at P/P^0 = 0.99	Average pore width (BJH) (nm)
$SBA15_{AS}$	159.42	0.10	—
$SBA15_{calc}$	927.63	1.01	8.98
LMO–SBA15	486.27	0.50	7.70
HMO–SBA15	638.82	0.65	7.69

3.6 Effect of pH on the adsorption capacity

It is well known that the pH is a crucial factor in adsorption processes.[36] This effect was studied using a pH range of 4 to 11. As shown in Fig. 5a, with the increase of pH from 4 to ∼7 the adsorption capacity rises to a peak of 14.2 mg g^{-1}, slightly decreasing to pH 11. At lower pH, H^+ competes with Li^+ for the adsorption sites, reducing the adsorption capacity. However, at pH ∼ 7, more sites are available for Li^+. While higher pH typically enhances adsorption, the graph shows a slight drop at elevated pH; this might be due to the partial dissolution or degradation of the spinel phase, where excessive OH^- leads to redox reactions causing structural damage.[66] Since the

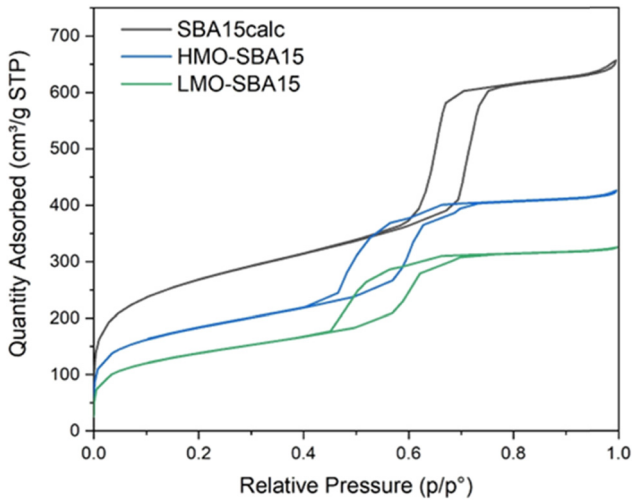

Fig. 3 Nitrogen adsorption–desorption isotherms of samples $SBA15_{calc}$, HMO–SBA15 and LMO–SBA15.

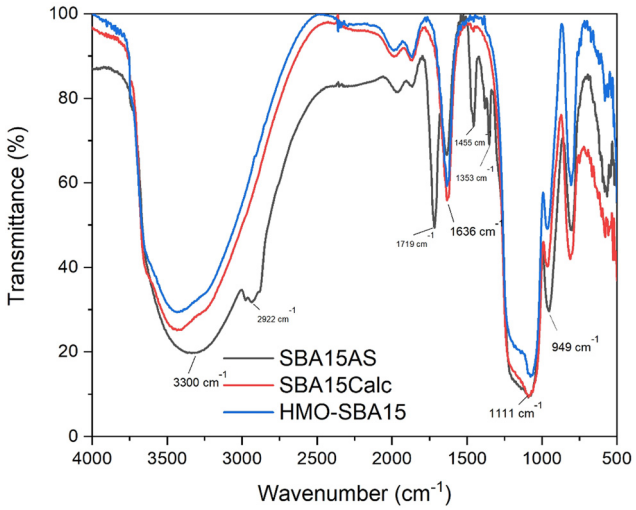

Fig. 4 FTIR spectral overlap of samples AS, calc and HMO.

 © 2025 The Author(s). Published by the Royal Society of Chemistry

Open Access Article. Published on 07 August 2025. Downloaded on 1/7/2026 11:10:38 PM.
This article is licensed under a Creative Commons Attribution-NonCommercial 3.0 Unported Licence.

maximum Q_e occurs at pH = 7, further experiments were conducted at this pH.

3.7 Effect of contact time and initial Li^+ concentration

The effect of contact time and initial Li^+ concentration was investigated at 10–1000 mg L^{-1}. The time to reach the equilibrium was around 6 hours. Most of the adsorption occurred in the first 60 minutes but it gradually reached equilibrium in the next 5 hours. It can be seen from Fig. 5b that the amount of adsorbed lithium increased with the increase in time and the initial lithium concentration up to 350 mg L^{-1}. For C_0 = 1000 mg L^{-1}, there is a clear decrease in adsorption (compared to C_0 = 350 mg L^{-1}), despite the higher initial concentration. The adsorption capacity reaches its maximum limit at C_0 = 350 mg L^{-1} and a further increase in Li^+ concentration does not lead to higher uptake; this can be a cause of saturation of adsorption sites, in which at lower and moderate concentrations the adsorbent surface has enough active sites to accommodate the Li^+ ions; however, at higher concentrations, the adsorption sites become saturated, and any additional Li^+ ions in the solution may not find available sites for adsorption.

3.8 Adsorption isotherm models

As a crucial parameter, the adsorption isotherm was usually applied to describe the distribution relationship between adsorbate molecules on the surface of adsorbents and residual quantity in the solution after adsorption. The Langmuir model is an ideal formula assuming that the surface of the adsorbent is homogenous and can only be covered with a complete monolayer. Meanwhile, all the activated sites are equivalent, and adsorbed molecules are independent of each other. Furthermore, the Freundlich model, as a widely used experiential equation, is based on multilayer adsorption with non-uniform distribution of adsorption heat and affinities over the heterogeneous surface.[67,68] The results of adsorption isotherms are presented in Table 2 and Fig. S7 (ESI†).

3.9 Adsorption kinetics

The experimental data of kinetic studies of lithium adsorption with different initial concentrations and at room temperature were fitted according to pseudo-first order and pseudo-second order models in Fig. 6. Table 3 shows the parameters for each model. As can be seen from this table, the theoretical adsorption capacity, $Q_{e,cal}$, obtained from the pseudo-second order model, was closer to the experimental value than that obtained from the pseudo-first order model. This shows that the pseudo-second order model is more suitable than the pseudo-first order model to predict the kinetic rate of the adsorption process.

One important aspect of the adsorption behavior of lithium ions on the SBA/HMO composite that requires attention is the influence of solution pH on the adsorption process. While the optimal pH was identified as ~7, changes in pH affected the adsorption capacity significantly, indicating that the composite's ion-exchange sites are sensitive to proton concentration. This raises questions about how the material will perform under real-world brine conditions, which often have fluctuating pH levels and competing ions that could influence adsorption efficiency.

The Langmuir isotherm model, which best fits the data, suggests a monolayer adsorption mechanism on a homogenous surface. This indicates that all adsorption sites on the SBA/HMO composite exhibit similar affinity for lithium ions, which is a desirable trait for efficient lithium recovery. However, the slight deviation from the Langmuir model observed at higher concentrations could suggest that surface heterogeneity or multilayer adsorption might occur at elevated ion levels. This opens the possibility of additional adsorption mechanisms, which should be explored in future studies to fully understand the behavior of the adsorbent under varying conditions.

In terms of kinetics, the superior fit of the pseudo-second-order model suggests that it is the dominant mechanism. This

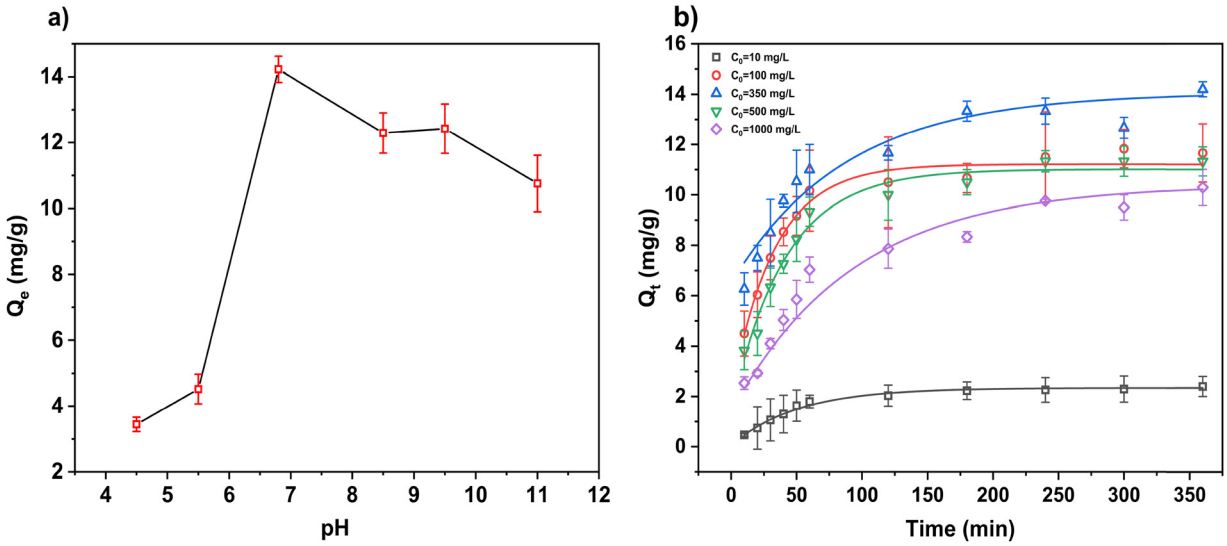

Fig. 5 (a) Effect of pH on the adsorption capacity of HMO–SBA15 and (b) effect of contact time and initial Li^+ concentration on the adsorption capacity.

Open Access Article. Published on 07 August 2025. Downloaded on 1/7/2026 11:10:38 PM.
This article is licensed under a Creative Commons Attribution-NonCommercial 3.0 Unported Licence.

Table 2 Isotherm parameters of the SBA/HMO adsorption

Langmuir model		
Q_m (mg g^{-1})	K_L (L mg^{-1})	R^2
13.77	5.29	0.98560
Freundlich model		
$1/n$	K_f (L g^{-1})	R^2
0.322	1.69	0.626

implies strong interactions between lithium ions and the active sites on the SBA/HMO composite, making it suitable for applications where selective ion adsorption is critical.

3.9.1 Desorption kinetics. Concentration data collected during batch experiments have been fitted with the reversible kinetic model described in Section 2.5.1. The maximum adsorption capacity of 13.77 mg g^{-1}, obtained from the study of the adsorption isotherms (Langmuir model), has been fixed for the fitting of all the observed data, while the values of the adsorption and desorption kinetic constants have been estimated during the procedure. The reversible second order kinetic model satisfactorily matches the experimental data, displaying determination coefficients close to 1 (Fig. 7).

Fig. 8 shows the value ranges of both second-order adsorption and desorption kinetic constants, which move within an order of magnitude of 10^{-5} (L mg^{-1} min^{-1}) and 10^{-3} (min^{-1}), respectively.

We are therefore dealing with a material having a finite number of active sites and featuring a significant desorption component. Furthermore, the decreasing trend of the latter with increasing concentration (Fig. 8) may be due to the greater competition caused by the higher number of ions that hinder each other in reaching the available active sites.

3.10 Adsorption selectivity

Under high ionic strength conditions (>110 g L^{-1} TDS), our HMO–SBA15 achieved rather good Li adsorption capacity with excellent selectivity. The reduced capacity compared to single-ion systems reflects the challenging multi-ion environment, where competing cations (particularly Na^+ at 61.9 g L^{-1}) and high ionic strength effects limit Li^+ accessibility to active sites. Despite these challenges, the HMO–SBA15 composite achieved separation factors of 1.8 for Li/Ca, 3.6 for Li/Mg, 5.9 for Li/K, and 7.4 for Li/Na, indicating progressively better selectivity for lithium over larger monovalent cations (Table 4). These values are consistent with the size-exclusion and electrostatic selectivity mechanisms inherent to hydrogen manganese oxide ion-sieves, where the spinel structure preferentially accommodates

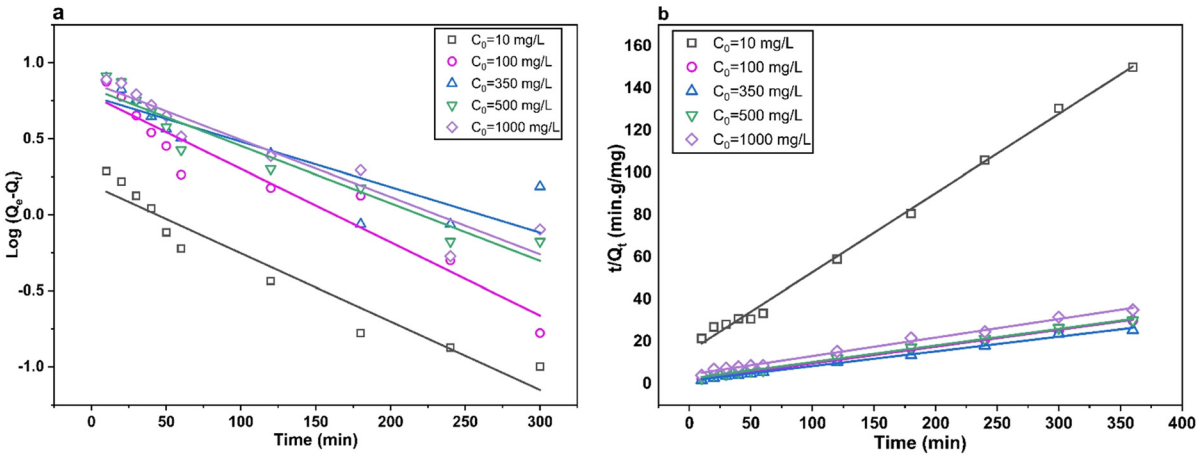

Fig. 6 (a) Pseudo-first and (b) second order models of the adsorption kinetics.

Table 3 Kinetic parameters of SBA/HMO in the adsorption process

		Initial concentration (mg L^{-1})				
Model	Parameter	10	100	350	500	1000
Pseudo-first order	K_f (min^{-1})	0.0092	0.0112	0.0069	0.0078	0.0085
	$Q_{e,cal}$ (mg g^{-1})	1.574	6.096	6.029	6.78	7.41
	R^2	0.9304	0.9252	0.7396	0.9226	0.9044
Pseudo-second order	K_2 (g mg^{-1} min^{-1})	0.0091	0.004	0.0037	0.0026	0.00181
	$Q_{e,cal}$ (mg g^{-1})	0.266	1.255	1.443	1.256	1.132
	R^2	0.9967	0.9984	0.9941	0.9974	0.9923

 © 2025 The Author(s). Published by the Royal Society of Chemistry

Open Access Article. Published on 07 August 2025. Downloaded on 1/7/2026 11:10:38 PM.
This article is licensed under a Creative Commons Attribution-NonCommercial 3.0 Unported Licence.

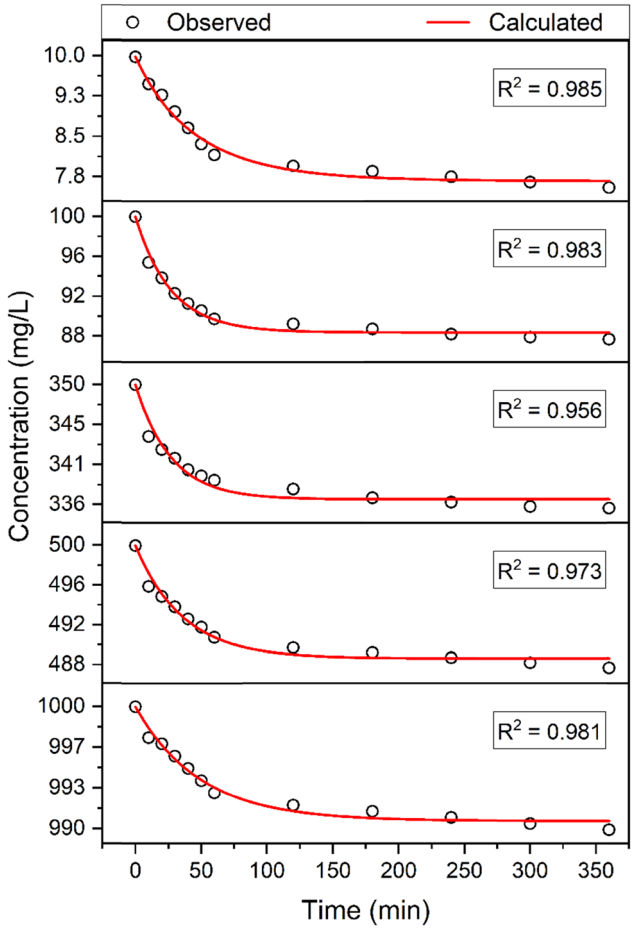

Fig. 7 Observed *vs.* calculated concentrations obtained with the reversible second order kinetic model applied to all batch tests.

lithium ions while discriminating against larger cations.[69,70] The moderate to good separation factors, particularly the excellent Li/Na selectivity of 7.4, demonstrate the material's practical potential for lithium recovery from complex brine systems.

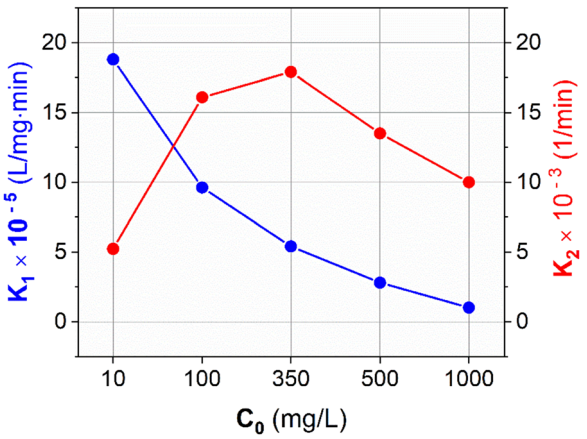

Fig. 8 Adsorption (K_1) and desorption (K_2) kinetic constant values estimated using the second-order kinetic model.

Table 4 Selectivity coefficients for the HMO–SBA15 adsorbent in the presence of competing cations

Cations	C_0 (mg L^{-1})	C_e (mg L^{-1})	K_d (L g^{-1})	α_M^{Li}
Li^+	3020	~2580	0.171	—
Na^+	61 900	~60 500	0.023	7.4
K^+	28 200	~27 400	0.029	5.9
Mg^{2+}	17 600	~16 800	0.048	3.6
Ca^{2+}	410	~375	0.093	1.8

3.11 Comparison with other adsorbents

In Table 5 Li sources, operating conditions and performances of different HMO crystals engineered in the form of composite adsorbents are presented.

It is noteworthy that among the materials reported, only two demonstrate a significantly higher adsorption efficiency than the material investigated in this study, specifically those described in ref. 71 and 73. However, despite the reported cost advantages of EP/HMO in the related reference, its synthesis involves multiple steps, such as granulation and porogen addition, which may limit scalability and increase complexity compared to simpler approaches, such as the SBA15 system. Similarly, the synthesis of HMO/PVA requires intricate procedures, including electrospinning and radiation-induced cross-linking, further contributing to production complexity and higher costs. Additionally, the performance of these materials is optimized at elevated pH values (*e.g.*, pH 10.1 for salt-lake brine), which may not be representative of all lithium-containing water sources. This necessitates additional chemical adjustments in less alkaline environments, further increasing operational costs and complicating large-scale implementation.

4. Conclusions

In conclusion, a novel SBA/HMO nanocomposite was developed and characterized for lithium ion capture from aqueous solutions. $Li_4Mn_5O_{12}$ was incorporated into $SBA15_{calc}$, followed by H^+ ion exchange, creating an effective ion-sieve adsorbent. Structural stability was confirmed through various analyses, including SEM and XRD.

The optimum pH for the maximum adsorption capacity of 14.2 mg g^{-1} was found to be pH 7, with the major lithium capture happening within the first 60 minutes, indicating a rapid ion exchange. The pseudo-second order kinetic model best fits the data. The selectivity order was $Li^+ \gg Na^+ > K^+ > Mg^{2+} > Ca^{2+}$. The reversible second-order kinetic model effectively describes the adsorption–desorption behavior of the material, revealing a finite number of active sites and faster desorption kinetics that highlight competitive ion effects at higher concentrations.

This composite shows promise as a sustainable alternative for lithium recovery, with an eco-friendly synthesis that avoids hazardous materials and enables recycling of the template. Its cost-effective and scalable process facilitates the production of larger quantities. However, the impact of varying pH under real brine conditions and the potential for additional adsorption

Open Access Article. Published on 07 August 2025. Downloaded on 1/7/2026 11:10:38 PM. This article is licensed under a Creative Commons Attribution-NonCommercial 3.0 Unported Licence.

Table 5 Li sources, operating conditions and performances of different HMO composite adsorbents

Adsorbent	Li source	C_0 (mg L^{-1})	pH	Q_e (mg g^{-1})	Ref.
EP[1]/HMO	Synthetic brine	>250	6.5–7	30.2	71
PVDF[2]/HMO spinning fiber	Geothermal water	200	12	14.95	72
HMO/PVA[3]	Salt lake brine	255.75	10.1	30.1	73
APTES[4]/HMO–HS	Synthetic brine	50	6	11.22	31
HMO	Synthetic brine	150	7.85	6.22	69
HMO	Geothermal brine	141	6.6	16.8	69
HMO–SBA15	Synthetic brine	350	~7	14.2	This work

EP: 1-epoxy resin-12; PVDF: 2-polyvinylidene fluoride; PVA: 3-polyvinyl alcohol; APTES: 4-3-aminopropyl-triethoxysilane.

mechanisms at higher concentrations warrant further investigation.

Author contributions

Keivan Sohrabpour: investigation, methodology, validation, visualization, writing – original draft, writing – review and editing; Antonio Grisolia: investigation, methodology, validation, visualization, writing – original draft, writing – review and editing; Francesco Chidichimo: writing – original draft; Pietro Argurio: formal analysis; Efrem Curcio: conceptualization, supervision; Salvatore Straface: conceptualization, funding acquisition, resources, supervision, writing – review & editing; Luigi Pasqua: conceptualization, resources, supervision, writing – review and editing.

Conflicts of interest

The authors declare that they have no known competing financial interests or personal relationships that could have appeared to influence the work reported in this paper.

Data availability

The data supporting this article have been included as part of the ESI.† Any further data required will be available upon request.

Acknowledgements

This research was funded by the grant from European Union and MIUR, FSE-REACT-EU NOP Research and Innovation fund (Axis IV, Action IV.4 and IV.5, CUP H29J21010100006, DOT1305053) and the Next Generation EU – Italian PNRR, Mission 4, Component 2, Investment 1.5, call for the creation and strengthening of 'Innovation Ecosystems', building 'Territorial R&D Leaders' (Directorial Decree no. 2021/3277) – project Tech4You – Technologies for climate change adaptation and quality of life improvement, no. ECS0000009. This work reflects only the authors' views and opinions, neither the Ministry for University and Research nor the European Commission can be considered responsible for them.

References

1 B. Scrosati and J. Garche, Lithium batteries: status, prospects and future, *J. Power Sources*, 2010, **195**, 2419–2430, DOI: 10.1016/j.jpowsour.2009.11.048.
2 B. Swain, Recovery and recycling of lithium: a review, *Sep. Purif. Technol.*, 2017, **172**, 388–403, DOI: 10.1016/J.SEPPUR.2016.08.031.
3 International Energy Agency (IEA), The Role of Critical Minerals in Clean Energy Transitions, 2021, https://www.iea.org/reports/the-role-of-critical-minerals-in-clean-energy-transitions (accessed July 29, 2024).
4 G. Zubi, R. Dufo-López, M. Carvalho and G. Pasaoglu, The lithium-ion battery: state of the art and future perspectives, *Renewable Sustainable Energy Rev.*, 2018, **89**, 292–308, DOI: 10.1016/j.rser.2018.03.002.
5 J. K. Rybakowski and C. K. Janusz Rybakowski, Lithium treatment in the era of personalized medicine, *Drug Dev. Res.*, 2021, **82**, 621–627, DOI: 10.1002/DDR.21660.
6 G. S. Malhi, M. Tanious, P. Das and M. Berk, The science and practice of lithium therapy, *Aust. N. Z. J. Psychiatry*, 2012, **46**, 192–211, DOI: 10.1177/0004867412437346/ASSET/IMAGES/LARGE/10.1177_0004867412437346-FIG6.JPEG.
7 G. S. Malhi, D. Gessler and T. Outhred, The use of lithium for the treatment of bipolar disorder: recommendations from clinical practice guidelines, *J. Affective Disord.*, 2017, **217**, 266–280, DOI: 10.1016/J.JAD.2017.03.052.
8 A. Ebensperger, P. Maxwell and C. Moscoso, The lithium industry: its recent evolution and future prospects, *Resour. Policy*, 2005, **30**, 218–231, DOI: 10.1016/j.resourpol.2005.09.001.
9 L. Talens Peiró, G. Villalba Méndez and R. U. Ayres, Lithium: sources, production, uses, and recovery outlook, *JOM*, 2013, **65**, 986–996, DOI: 10.1007/s11837-013-0666-4.
10 P. Meshram, B. D. Pandey and T. R. Mankhand, Extraction of lithium from primary and secondary sources by pretreatment, leaching and separation: a comprehensive review, *Hydrometallurgy*, 2014, **150**, 192–208, DOI: 10.1016/j.hydromet.2014.10.012.
11 V. Flexer, C. F. Baspineiro and C. I. Galli, Lithium recovery from brines: a vital raw material for green energies with a potential environmental impact in its mining and processing, *Sci. Total Environ.*, 2018, **639**, 1188–1204, DOI: 10.1016/j.scitotenv.2018.05.223.
12 D. Yelatontsev and A. Mukhachev, Processing of lithium ores: industrial technologies and case studies – A review,

 © 2025 The Author(s). Published by the Royal Society of Chemistry

Open Access Article. Published on 07 August 2025. Downloaded on 1/7/2026 11:10:38 PM.
This article is licensed under a Creative Commons Attribution-NonCommercial 3.0 Unported Licence.

Hydrometallurgy, 2021, **201**, 105578, DOI: 10.1016/j.hydromet.2021.105578.

13 H. Li, J. Eksteen and G. Kuang, Recovery of lithium from mineral resources: state-of-the-art and perspectives – A review, *Hydrometallurgy*, 2019, **189**, 105129, DOI: 10.1016/j.hydromet.2019.105129.

14 A. Battistel, M. S. Palagonia, D. Brogioli, F. La Mantia and R. Trócoli, Electrochemical Methods for Lithium Recovery: A Comprehensive and Critical Review, *Adv. Mater.*, 2020, **32**(23), DOI: 10.1002/adma.201905440.

15 W. T. Stringfellow and P. F. Dobson, Technology for the Recovery of Lithium from Geothermal Brines, *Energies*, 2021, **14**, 6805, DOI: 10.3390/en14206805.

16 R. Reich, K. Slunitschek, R. M. Danisi, E. Eiche and J. Kolb, Lithium Extraction Techniques and the Application Potential of Different Sorbents for Lithium Recovery from Brines, *Miner. Process. Extr. Metall. Rev.*, 2023, **44**, 261–280, DOI: 10.1080/08827508.2022.2047041.

17 S. H. Park, J. H. Kim, S. J. Moon, J. T. Jung, H. H. Wang, A. Ali, C. A. Quist-Jensen, F. Macedonio, E. Drioli and Y. M. Lee, Lithium recovery from artificial brine using energy-efficient membrane distillation and nanofiltration, *J. Membr. Sci.*, 2020, **598**, 117683, DOI: 10.1016/j.memsci.2019.117683.

18 X. Li, Y. Mo, W. Qing, S. Shao, C. Y. Tang and J. Li, Membrane-based technologies for lithium recovery from water lithium resources: a review, *J. Membr. Sci.*, 2019, **591**, 117317, DOI: 10.1016/j.memsci.2019.117317.

19 Q. Yu, E. Morioka and K. Sasaki, Characterization of lithium ion sieve derived from biogenic Mn oxide, *Microporous Mesoporous Mater.*, 2013, **179**, 122–127, DOI: 10.1016/j.micromeso.2013.05.026.

20 B. N. S. Al-dhawi, S. R. M. Kutty, L. Baloo, A. M. Alawag, N. M. Y. Almahbashi, G. M. A. Naji, Y. A. A. Alsaeedi, F. A. H. Al-Towayti and A. H. Jagaba, Lithium adsorption from aqueous solution using aluminum hydroxide: characterization, optimization by response surface methodology, kinetic modelling, and isotherm studies, *Case Stud. Chem. Environ. Eng.*, 2023, **7**, 100350, DOI: 10.1016/j.cscee.2023.100350.

21 M. L. Vera, W. R. Torres, C. I. Galli, A. Chagnes and V. Flexer, Environmental impact of direct lithium extraction from brines, *Nat. Rev. Earth Environ.*, 2023, **4**, 149–165, DOI: 10.1038/s43017-022-00387-5.

22 R. Cantillana and I. Iniesta-Arandia, Beyond scarcity and its management: sociocultural dimensions of the water crisis in the Atacama Desert, *Water Policy*, 2022, **24**, 1124–1145, DOI: 10.2166/wp.2022.297.

23 G. Lagos, L. Cifuentes, D. Peters, L. Castro and J. M. Valdés, Carbon footprint and water inventory of the production of lithium in the Atacama Salt Flat, Chile, *Environ. Challenges*, 2024, **16**, 100962, DOI: 10.1016/j.envc.2024.100962.

24 M. Mureseanu, A. Reiss, I. Stefanescu, E. David, V. Parvulescu, G. Renard and V. Hulea, Modified SBA-15 mesoporous silica for heavy metal ions remediation, *Chemosphere*, 2008, **73**, 1499–1504, DOI: 10.1016/j.chemosphere.2008.07.039.

25 L. Tang, S. Huang, Y. Wang, D. Liang, Y. Li, J. Li, Y. Wang, Y. Xie and W. Wang, Highly Efficient, Stable, and Recyclable Hydrogen Manganese Oxide/Cellulose Film for the Extraction of Lithium from Seawater, *ACS Appl. Mater. Interfaces*, 2020, **12**, 9775–9781, DOI: 10.1021/acsami.9b21612.

26 H.-J. Hong, T. Ryu, I.-S. Park, M. Kim, J. Shin, B.-G. Kim and K.-S. Chung, Highly porous and surface-expanded spinel hydrogen manganese oxide (HMO)/Al_2O_3 composite for effective lithium (Li) recovery from seawater, *Chem. Eng. J.*, 2018, **337**, 455–461, DOI: 10.1016/j.cej.2017.12.130.

27 H.-J. Hong, I.-S. Park, J. Ryu, T. Ryu, B.-G. Kim and K.-S. Chung, Immobilization of hydrogen manganese oxide (HMO) on alpha-alumina bead (AAB) to effective recovery of Li^+ from seawater, *Chem. Eng. J.*, 2015, **271**, 71–78, DOI: 10.1016/j.cej.2015.02.023.

28 P. N. E. Diagboya and E. D. Dikio, Silica-based mesoporous materials; emerging designer adsorbents for aqueous pollutants removal and water treatment, *Microporous Mesoporous Mater.*, 2018, **266**, 252–267, DOI: 10.1016/j.micromeso.2018.03.008.

29 M. C. Bourkaib, P. Gaudin, F. Vibert, Y. Guiavarc'h, S. Delaunay, X. Framboisier, C. Humeau, I. Chevalot and J.-L. Blin, APTES modified SBA15 and meso-macro silica materials for the immobilization of aminoacylases from Streptomyces ambofaciens, *Microporous Mesoporous Mater.*, 2021, **323**, 111226, DOI: 10.1016/j.micromeso.2021.111226.

30 D. Zhao, J. Feng, Q. Huo, N. Melosh, G. H. Fredrickson, B. F. Chmelka and G. D. Stucky, Triblock Copolymer Syntheses of Mesoporous Silica with Periodic 50 to 300 Angstrom Pores, *Science*, 1998, **279**, 548–552, DOI: 10.1126/science.279.5350.548.

31 Y. Wang, J. Xu, X. Xu, D. Yang, X. Zheng, J. Pan, T. Zhang, F. Qiu and C. Li, Mesoporous hollow silicon spheres modified with manganese ion sieve: preparation and its application for adsorption of lithium and rubidium ions, *Appl. Organomet. Chem.*, 2018, **32**(3), DOI: 10.1002/aoc.4182.

32 M. S. Anantha, S. Olivera, C. Hu, B. K. Jayanna, N. Reddy, K. Venkatesh, H. B. Muralidhara and R. Naidu, Comparison of the photocatalytic, adsorption and electrochemical methods for the removal of cationic dyes from aqueous solutions, *Environ. Technol. Innov.*, 2020, **17**, 100612, DOI: 10.1016/j.eti.2020.100612.

33 N. M. Mahmoodi, U. Sadeghi, A. Maleki, B. Hayati and F. Najafi, Synthesis of cationic polymeric adsorbent and dye removal isotherm, kinetic and thermodynamic, *J. Ind. Eng. Chem.*, 2014, **20**, 2745–2753, DOI: 10.1016/j.jiec.2013.11.002.

34 S. Wang, P. Li, X. Zhang, S. Zheng and Y. Zhang, Selective adsorption of lithium from high Mg-containing brines using H_xTiO_3 ion sieve, *Hydrometallurgy*, 2017, **174**, 21–28, DOI: 10.1016/j.hydromet.2017.09.009.

35 L. Wu, C. Zhang, S. Kim, T. A. Hatton, H. Mo and T. D. Waite, Lithium recovery using electrochemical technologies: advances and challenges, *Water Res.*, 2022, **221**, 118822, DOI: 10.1016/j.watres.2022.118822.

36 M. A. Al-Ghouti and D. A. Da'ana, Guidelines for the use and interpretation of adsorption isotherm models: a review,

Open Access Article. Published on 07 August 2025. Downloaded on 1/7/2026 11:10:38 PM.
This article is licensed under a Creative Commons Attribution-NonCommercial 3.0 Unported Licence.

J. Hazard. Mater., 2020, **393**, 122383, DOI: 10.1016/j.jhazmat.2020.122383.

37 J. Wang and X. Guo, Adsorption isotherm models: classification, physical meaning, application and solving method, *Chemosphere*, 2020, **258**, 127279, DOI: 10.1016/j.chemosphere.2020.127279.

38 K. Sohrabpour, S. Mohamadi, E. Abdollahzadeh Sharghi and M. Abdouss, Performance evaluation of novel Mica@reduced graphene oxide fixed rotating disk reactor in treatment of anaerobically reduced textile dyeing wastewater containing aromatic amines, *J. Chem. Technol. Biotechnol.*, 2021, **96**, 2072–2085, DOI: 10.1002/jctb.6742.

39 X. Li, L. Chen, Y. Chao, W. Chen, J. Luo, J. Xiong, F. Zhu, X. Chu, H. Li and W. Zhu, Amorphous TiO_2-Derived Large-Capacity Lithium Ion Sieve for Lithium Recovery, *Chem. Eng. Technol.*, 2020, **43**, 1784–1791, DOI: 10.1002/ceat.201900374.

40 A. Ayub, Z. A. Raza, M. I. Majeed, M. R. Tariq and A. Irfan, Development of sustainable magnetic chitosan biosorbent beads for kinetic remediation of arsenic contaminated water, *Int. J. Biol. Macromol.*, 2020, **163**, 603–617, DOI: 10.1016/j.ijbiomac.2020.06.287.

41 S. Lagergren, Zur theorie der sogenannten adsorption gelöster stoffe Kungliga Svenska Vetenskapsakademiens, *Handlingar*, 1898, **24**, 1–39.

42 Y. Ho, Review of second-order models for adsorption systems, *J. Hazard. Mater.*, 2006, **136**, 681–689, DOI: 10.1016/j.jhazmat.2005.12.043.

43 F. Chidichimo, M. De Biase, A. Tursi, M. Maiolo, S. Straface, M. Baratta, F. Olivito and G. De Filpo, A model for the adsorption process of water dissolved elements flowing into reactive porous media: characterization and sizing of water mining/filtering systems, *J. Hazard. Mater.*, 2023, **445**, 130554, DOI: 10.1016/j.jhazmat.2022.130554.

44 Y. Han, H. Kim and J. Park, Millimeter-sized spherical ion-sieve foams with hierarchical pore structure for recovery of lithium from seawater, *Chem. Eng. J.*, 2012, **210**, 482–489, DOI: 10.1016/j.cej.2012.09.019.

45 C. Biagioni and M. Pasero, The systematics of the spinel-type minerals: an overview, *Am. Mineral.*, 2014, **99**, 1254–1264, DOI: 10.2138/am.2014.4816.

46 J.-L. Xiao, S.-Y. Sun, J. Wang, P. Li and J.-G. Yu, Synthesis and Adsorption Properties of $Li_{1.6}Mn_{1.6}O_4$ Spinel, *Ind. Eng. Chem. Res.*, 2013, **52**, 11967–11973, DOI: 10.1021/ie400691d.

47 D. Weng, H. Duan, Y. Hou, J. Huo, L. Chen, F. Zhang and J. Wang, Introduction of manganese based lithium-ion Sieve-A review, *Prog. Nat. Sci.: Mater. Int.*, 2020, **30**, 139–152, DOI: 10.1016/j.pnsc.2020.01.017.

48 F. Qian, M. Guo, Z. Qian, Q. Li, Z. Wu and Z. Liu, Highly Lithium Adsorption Capacities of $H_{1.6}Mn_{1.6}O_4$ Ion-Sieve by Ordered Array Structure, *ChemistrySelect*, 2019, **4**, 10157–10163, DOI: 10.1002/slct.201902173.

49 K. Shi, M. Luo, J. Ying, S. Zhen, Z. Xing and R. Chen, Extraction of Lithium from Single-Crystalline Lithium Manganese Oxide Nanotubes Using Ammonium Peroxodisulfate, *iScience*, 2020, **23**, 101768, DOI: 10.1016/j.isci.2020.101768.

50 R. Sanz, G. Calleja, A. Arencibia and E. S. Sanz-Pérez, Amino functionalized mesostructured SBA-15 silica for CO_2 capture: exploring the relation between the adsorption capacity and the distribution of amino groups by TEM, *Microporous Mesoporous Mater.*, 2012, **158**, 309–317, DOI: 10.1016/j.micromeso.2012.03.053.

51 A. Katiyar, S. Yadav, P. G. Smirniotis and N. G. Pinto, Synthesis of ordered large pore SBA-15 spherical particles for adsorption of biomolecules, *J. Chromatogr. A*, 2006, **1122**, 13–20, DOI: 10.1016/j.chroma.2006.04.055.

52 H. I. Lee, J. H. Kim, G. D. Stucky, Y. Shi, C. Pak and J. M. Kim, Morphology-selective synthesis of mesoporous SBA-15 particles over micrometer, submicrometer and nanometer scales, *J. Mater. Chem.*, 2010, **20**, 8483, DOI: 10.1039/c0jm00820f.

53 F. E. da Silva, E. Rigoti, M. I. S. de Mello and S. B. C. Pergher, Tuning Textural Properties by Changing the Morphology of SBA-15 Mesoporous Materials, *Materials*, 2024, **17**, 2827, DOI: 10.3390/ma17122827.

54 P. Shah and V. Ramaswamy, Thermal stability of Mesoporous SBA-15 and Sn-SBA-15 Molecular Sieves: an in situ HTXRD study, *Microporous Mesoporous Mater.*, 2008, **114**, 270–280, DOI: 10.1016/j.micromeso.2008.01.013.

55 C. Wang, S. Lim, G. Du, C. Z. Loebicki, N. Li, S. Derrouiche and G. L. Haller, Synthesis, Characterization, and Catalytic Performance of Highly Dispersed Co-SBA-15, *J. Phys. Chem. C*, 2009, **113**, 14863–14871, DOI: 10.1021/jp901823v.

56 S. G. Mohamed, S. Y. Attia and H. H. Hassan, Spinel-structured $FeCo_2O_4$ mesoporous nanosheets as efficient electrode for supercapacitor applications, *Microporous Mesoporous Mater.*, 2017, **251**, 26–33, DOI: 10.1016/j.micromeso.2017.05.035.

57 F. Marchini, D. Rubi, M. del Pozo, F. J. Williams and E. J. Calvo, Surface Chemistry and Lithium-Ion Exchange in $LiMn_2O_4$ for the Electrochemical Selective Extraction of LiCl from Natural Salt Lake Brines, *J. Phys. Chem. C*, 2016, **120**, 15875–15883, DOI: 10.1021/acs.jpcc.5b11722.

58 P. Ji, Y. Xi, C. Zhang, C. Wang, C. Hu, Y. Guan and D. Zhang, Waxberry-Like Nanosphere $Li_4Mn_5O_{12}$ as High Performance Electrode Materials for Supercapacitors, *J. Low Power Electron. Appl.*, 2018, **8**, 32, DOI: 10.3390/jlpea8030032.

59 M. Thommes, K. Kaneko, A. V. Neimark, J. P. Olivier, F. Rodriguez-Reinoso, J. Rouquerol and K. S. W. Sing, Physisorption of gases, with special reference to the evaluation of surface area and pore size distribution (IUPAC Technical Report), *Pure Appl. Chem.*, 2015, **87**, 1051–1069, DOI: 10.1515/pac-2014-1117.

60 F. X. Wang, S. Y. Xiao, X. W. Gao, Y. S. Zhu, H. P. Zhang, Y. P. Wu and R. Holze, Nanoporous $LiMn_2O_4$ spinel prepared at low temperature as cathode material for aqueous supercapacitors, *J. Power Sources*, 2013, **242**, 560–565, DOI: 10.1016/j.jpowsour.2013.05.115.

61 M. J. Young, S. Letourneau, R. E. Warburton, W. M. Dose, C. Johnson, J. Greeley and J. W. Elam, High-Rate Spinel $LiMn_2O_4$ (LMO) Following Carbonate Removal and Formation of Li-Rich Interface by ALD Treatment, *J. Phys.*

 © 2025 The Author(s). Published by the Royal Society of Chemistry

Open Access Article. Published on 07 August 2025. Downloaded on 1/7/2026 11:10:38 PM.
This article is licensed under a Creative Commons Attribution-NonCommercial 3.0 Unported Licence.

Chem. C, 2019, **123**, 23783–23790, DOI: 10.1021/acs.jpcc.9b04418.

62 A. Alessi, S. Agnello, G. Buscarino and F. M. Gelardi, Raman and IR investigation of silica nanoparticles structure, *J. Non-Cryst. Solids*, 2013, **362**, 20–24, DOI: 10.1016/j.jnoncrysol.2012.11.006.

63 D. Pérez-Quintanilla, A. Sánchez, I. del Hierro, M. Fajardo and I. Sierra, Synthesis and Characterization of Novel Mesoporous Silicas of the MSU-X Family for Environmental Applications, *J. Nanosci. Nanotechnol.*, 2009, **9**, 4901–4909, DOI: 10.1166/jnn.2009.1106.

64 M. D. Rami, M. Taghizadeh and H. Akhoundzadeh, Synthesis and characterization of nano-sized hierarchical porous AuSAPO-34 catalyst for MTO reaction: special insight on the influence of TX-100 as a cheap and green surfactant, *Microporous Mesoporous Mater.*, 2019, **285**, 259–270, DOI: 10.1016/j.micromeso.2019.05.028.

65 B. Zhang, L. Zhou, M. Qi, Z. Li, J. Han, K. Li, Y. Zhang, F. Dehghani, R. Liu and J. Yun, Outstanding Stability and Enhanced Catalytic Activity for Toluene Oxidation by Si–O–Mn Interaction over MnO_x/SiO_2, *Ind. Eng. Chem. Res.*, 2022, **61**, 1044–1055, DOI: 10.1021/acs.iecr.1c02504.

66 Q. Liu, L. Zhang, X. Liu, Z. Zhong, W. Deng and P. Yang, The preparation path, adsorption characteristics and manganese dissolution loss mechanism of manganese-based ion-sieve $MnO_2{\cdot}0.5H_2O$ for liquid phase lithium resource recovery, *J. Environ. Chem. Eng.*, 2025, **13**, 115154, DOI: 10.1016/j.jece.2024.115154.

67 L. Wang, C. G. Meng, M. Han and W. Ma, Lithium uptake in fixed-pH solution by ion sieves, *J. Colloid Interface Sci.*, 2008, **325**, 31–40, DOI: 10.1016/j.jcis.2008.05.005.

68 Q. Song, J. Liang, Y. Fang, C. Cao, Z. Liu, L. Li, Y. Huang, J. Lin and C. Tang, Selective adsorption behavior/mechanism of antibiotic contaminants on novel boron nitride bundles, *J. Hazard. Mater.*, 2019, **364**, 654–662, DOI: 10.1016/j.jhazmat.2018.10.054.

69 L. Herrmann, H. Ehrenberg, M. Graczyk-Zajac, E. Kaymakci, T. Kölbel, L. Kölbel and J. Tübke, Lithium recovery from geothermal brine – an investigation into the desorption of lithium ions using manganese oxide adsorbents, *Energy Adv.*, 2022, **1**, 877–885, DOI: 10.1039/D2YA00099G.

70 K. Ooi, Y. Miyai and S. Katoh, Recovery of Lithium from Seawater by Manganese Oxide Adsorbent, *Sep. Sci. Technol.*, 1986, **21**, 755–766, DOI: 10.1080/01496398608056148.

71 X. Lai, Y. Yuan, Z. Chen, J. Peng, H. Sun and H. Zhong, Adsorption–Desorption Properties of Granular EP/HMO Composite and Its Application in Lithium Recovery from Brine, *Ind. Eng. Chem. Res.*, 2020, **59**, 7913–7925, DOI: 10.1021/acs.iecr.0c00668.

72 H. Li, J. Qin, K. Zhao, Y. Guo, B. Tong, M. Samadiy, U. Alimov and T. Deng, Novel lithium ion-sieve spinning fiber composite of PVDF-HMO for lithium recovery from geothermal water, *J. Cleaner Prod.*, 2024, **434**, 139997, DOI: 10.1016/j.jclepro.2023.139997.

73 S. Qi, L. Xu, H. Shao, C. Huang, L. Ma, J. Han, X. Xue, M. Zhang and H. Ma, Cross-linked HMO/PVA nanofiber mats for efficient lithium extraction from Salt-lake, *Sep. Purif. Technol.*, 2023, **323**, 124382, DOI: 10.1016/j.seppur.2023.124382.